ACS APPLIED MATERIALS & INTERFACES
Research Article
www.acsami.org

Novel ZnO/Fe_2O_3 Core–Shell Nanowires for Photoelectrochemical Water Splitting

Yu-Kuei Hsu,*[†] Ying-Chu Chen,[‡] and Yan-Gu Lin*[§]

[†]Department of Optoelectronic Engineering, National Dong Hwa University, Hualien 97401, Taiwan
[‡]Karlsruhe Institute of Technology (KIT), Institut für Anorganische Chemie, Engesserstraße 15, Karlsruhe D-76131, Germany
[§]National Synchrotron Radiation Research Center, Hsinchu 30076, Taiwan

Supporting Information

ABSTRACT: A facile and simple fabrication of Fe_2O_3 as a shell layer on the surface of ZnO nanowires (NW) as a core–shell nanoelectrode is applied for the photoelectrochemical (PEC) splitting of water. An ZnO NW array of core diameter ~80 nm was grown on a fluorine-doped tin-oxide (FTO) substrate with a hydrothermal method; subsequent deposition and annealing achieved a shell structure of the Fe_2O_3 layer of thickness a few nm. Fe_2O_3 in the α phase and ZnO in the wurtzite phase were identified as the structures of the shell and core, respectively, through analysis with X-ray diffraction, scanning electron microscopy, and transmission electron microscopy. The ZnO/Fe_2O_3 core–shell NW showed an excellent PEC response to the oxidation of water, and also benefited from a negative shift of onset potential because of an n/n heterojunction structure. A detailed energy diagram of the ZnO/Fe_2O_3 core–shell NW was investigated with a Mott–Schottky analysis. This novel core–shell nanostructure can hence not only exhibit a great potential for the solar generation of hydrogen, but also offer a blueprint for the future design of photocatalysts.

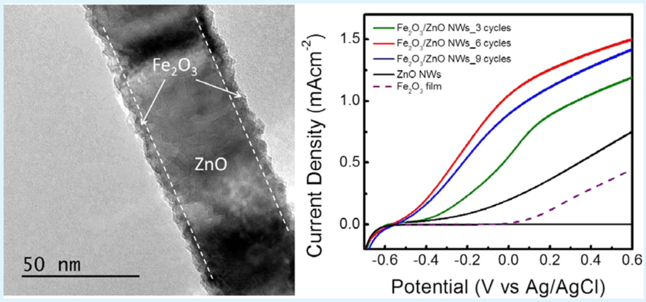

KEYWORDS: *zinc oxide, iron oxide, core–shell nanowires, photoelectrochemical, solar hydrogen*

1. INTRODUCTION

Fossil fuels constitute a finite resource on this planet and cause serious environmental concerns associated with combustion. Because of these urgent considerations of energy and environmental requirements, techniques to generate renewable energy with zero carbon emission must be developed. Among clean methods to produce energy, hydrogen is considered to be an environmentally amenable fuel for the future; a photoelectrochemical (PEC) system to split water offers a promising route to produce hydrogen from water with sustainable solar energy at a semiconductor–electrolyte interface.[1–4] Most research has been focused on such photoactive materials as photoelectrodes as TiO_2, GaN, InGaN, WO_3, and ZnO that have a wide band gap, and that must thus be modified to shift that energy band gap, by doping with a substitutional element to extend the photoresponse to visible light.[5–9] The inherently unavoidable trap centers that are created by dopants significantly decrease; however, their photoresponse, the limited solubility of dopants also hampers the shrinkage of the band gap in those photoactive materials. Iron oxide in the α-phase (α-Fe_2O_3) with a band gap 2.2 eV hence attracts increasing attention for the conversion of solar energy because iron is an abundant and cheap material.[10–12] Highly active photoanodes of α-Fe_2O_3 nanostructures within nanoparticle aggregates have achieved photocurrent 4 mA cm^{-2} at potential 1.53 V vs RHE.[13] These results reveal the great potential of α-Fe_2O_3 for the PEC decomposition of water; this large PEC activity can become enhanced with the use of materials of nanometer size, which are particularly relevant on account of their large ratio of surface to volume and small diffusion length for carrier transport, compared with their bulk counterparts.[13] α-Fe_2O_3 photoanodes show a positive onset potential of 0.9 V vs RHE, which results in a requirement of an external voltage to achieve water splitting, as the energy of the conduction band is too small for water reduction.[14–16] A small diffusion length, L_D = 2–4 nm, of minority carriers in this α-Fe_2O_3 material would limit its effective thickness and light absorption.[16] On the basis of these concerns, an investigation targeted on core–shell nanostructures for PEC generation of hydrogen might concurrently provide an alternative route to engineer the band position of α-Fe_2O_3 with heterojunction structures, and achieve an efficient utilization of α-Fe_2O_3 with a thin shell-layer structure.[17,18] In this work, we propose a facile and simple fabrication of α-Fe_2O_3 as a shell layer on the surface of ZnO nanowires (NW) as a core–shell nanoelectrode for application to the PEC splitting of water. The optimal PEC activities of ZnO/Fe_2O_3 core–shell NW as photoanodes are systematically analyzed. These novel ZnO/Fe_2O_3 core–shell NW arrays not

Received: May 6, 2015
Accepted: June 8, 2015
Published: June 8, 2015

DOI: 10.1021/acsami.5b03921
ACS Appl. Mater. Interfaces 2015, 7, 14157–14162

Scheme 1. Synthesis of ZnO/Fe_2O_3 Core−Shell NW Array

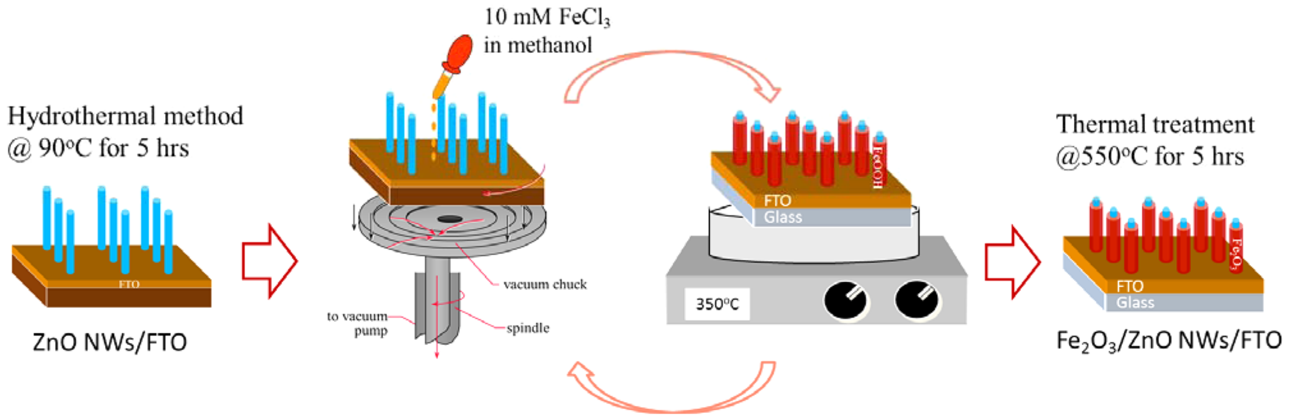

only function as photoanodes for the PEC generation of hydrogen, but also offer an opportunity to develop electronic and photoelectronic devices based on 3D-hierarchical nanomaterials.

2. EXPERIMENTAL SECTION

ZnO/Fe_2O_3 core−shell NW arrays on glass substrates coated with fluorine-doped tin oxide (FTO) were synthesized with a simple wet-chemical process, shown in Scheme 1. The first step was the formation of ZnO NW with a hydrothermal method. A layer (thickness 10−15 nm) of ZnO nanoparticles was deposited onto a substrate seeded with FTO on dip coating of a zinc-acetate solution (0.005 M) and thermal treatment at 350 °C for 5 min in air. The seeded substrate was placed in an aqueous solution containing zinc nitrate (0.005 M), hexamethylenetetramine (HMTA, 0.005 M), polyethylenimine (PEI, 0.005 M), and ammonia (0.25 M) at 90 °C for 5 h for the growth of the ZnO NW array. The $FeCl_3$ solution (0.02 M in ethanol) was dropwise deposited onto the ZnO NW array and spin-dried at 3000 rpm after 30 s. The dried sample was subsequently heated on a hot plate in air at 350 °C for 5 min. This procedure of deposition and annealing is denoted as one cycle, and cycles of varied number were tested. The core−shell NW as prepared were further annealed in air at 550 °C for 4 h.

The morphology of the ZnO/Fe_2O_3 core−shell NW arrays was examined with a scanning electron microscope (SEM, JEM-4000EX); the structure of the samples was analyzed with an X-ray diffractometer (XRD, at a beamline 17B in NSRRC). The chemical states of the elements were determined with X-ray photoelectron spectra (XPS, at a beamline 24A in NSRRC). The detailed microscopic structure and the chemical composition of the ZnO/Fe_2O_3 core−shell heterostructures were investigated with high-resolution scanning transmission electron microscopy (HR-STEM, JEM2010F, and JEM2200FS operated at 200 kV, JEOL). The photoelectrochemical behavior of the electrodes was measured in NaOH solution (1 M) with a potentiostat/galvanostat (CHI 6273D). A conventional three-electrode system consisting of the ZnO/Fe_2O_3 core−shell NW array as the working electrode, a square platinum sheet as the auxiliary electrode, and an Ag/AgCl reference electrode in KCl solution (3 M) was implemented. All potentials reported in this article are relative to Ag/AgCl (3 M KCl, 0.207 V vs RHE). An Xe lamp (150 W) was used with an AM 1.5 filter (in Supporting Information, SI, Figure S1); the intensity of illumination at the sample position was determined to be 100 mW cm^{-2}. A monochromator (equipped with a Xe lamp, 150 W) provided monochromatic light for excitation to measure the efficiency of conversion of incident photons to electrons. The light was incident on the ZnO/Fe_2O_3 core−shell NW electrodes from the front face, through a quartz window and the electrolyte, unless otherwise noted.

3. RESULTS AND DISCUSSION

3.1. Structural and Composition Characterizations.

Figure 1, parts a and b, shows the surface morphologies of ZnO NW arrays synthesized via the hydrothermal method in a top view and a cross-sectional view. The dense and straight NW structures cover uniformly and compactly a large area of the

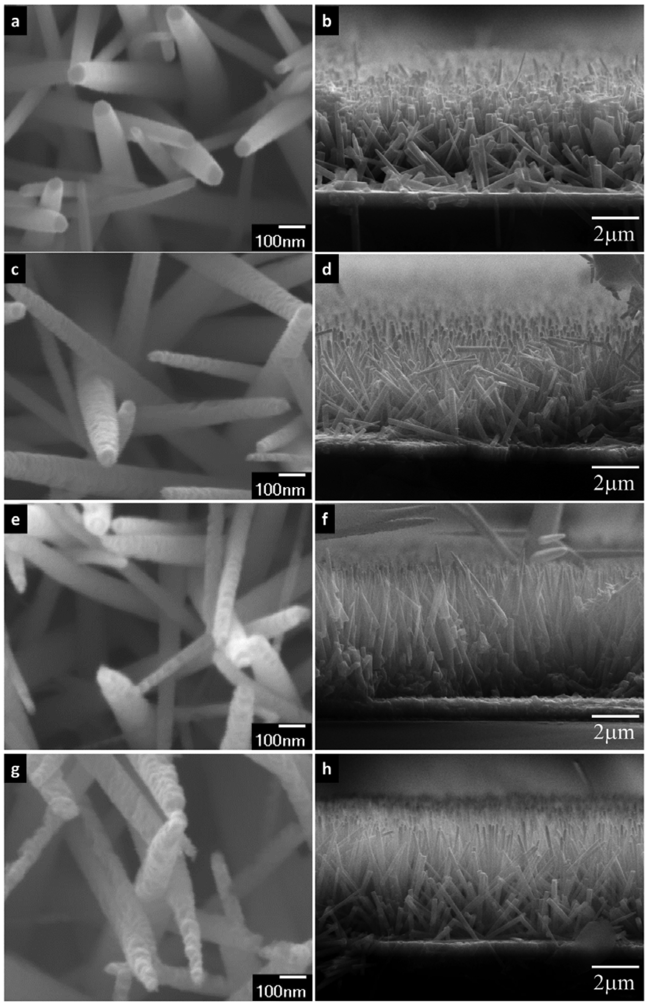

Figure 1. (a, b) FESEM images of ZnO NWs; SEM images of ZnO/Fe_2O_3 core−shell NWs at (c, d) 3 cycles, (e, f) 6 cycles, and (g, h) 9 cycles of deposition−annealing procedure.

FTO substrate; the NWs have lengths over 4 μm and diameter 50−80 nm. The ZnO NW samples as grown were then subjected to deposition and annealing for 3, 6, and 9 cycles; those samples were subsequently annealed at 550 °C for 5 h. The morphologic evolutions of those samples are displayed in Figure 1c−h, in which the uniform and thin layers of deposits on the ZnO NW surface relative to the pristine one are clearly observable. As the number of cycles of deposition and annealing increased, the thickness and roughness of the surface layer substantially increased, which implied that the thickness of the shell layer was adjustable with the number of cycles of that deposition and annealing. The lengths and density of all core−shell NW samples remained notably constant, which indicates that the procedure involving deposition and annealing does not significantly damage the ZnO NW.

XRD analysis was performed to study the crystal structure of the core−shell NW array samples for varied cycles of deposition and annealing, as shown in Figure 2a; the XRD pattern of pristine ZnO NW is displayed for comparison. As is observable, after increasing the number of cycles to nine, the three weak signals due to (012), (104), and (110) slightly appeared, clearly demonstrating the formation of α-Fe_2O_3 (hematite, JCPDS no. 33-0664) in the product. The weakness of the diffraction intensities of α-Fe_2O_3 indicate the deposition of an only thin layer, but the diffraction signals of ZnO NW remained, which confirms the fabrication of ZnO/Fe_2O_3 core−shell NW arrays. From the recorded XPS, the Fe 2p core-level spectra of core−shell samples were resolved as shown in Figure 2b. After depositions of 3, 6, and 9 cycles, the Fe 2p lines at 711.3 and 724.7 eV, corresponding to Fe $2p_{3/2}$ and $2p_{1/2}$, reveal an oxidation state of 3+. A satellite line of the Fe $2p_{3/2}$ main line is observed at approximately 719 eV, at an energy approximately 8 eV less than that of the main line, which is most likely indicative of the presence of Fe^{3+} species.[19] The Zn 2p core-level spectra of the samples after deposition for 3, 6, and 9 cycles were also recorded; their ratios of elemental composition of Zn to Fe were 9.0, 4.6, and 3.5, respectively. This result indicates that the deposition of the α-Fe_2O_3 layer significantly increased as the number of cycles increased, supporting the findings from SEM and XRD.

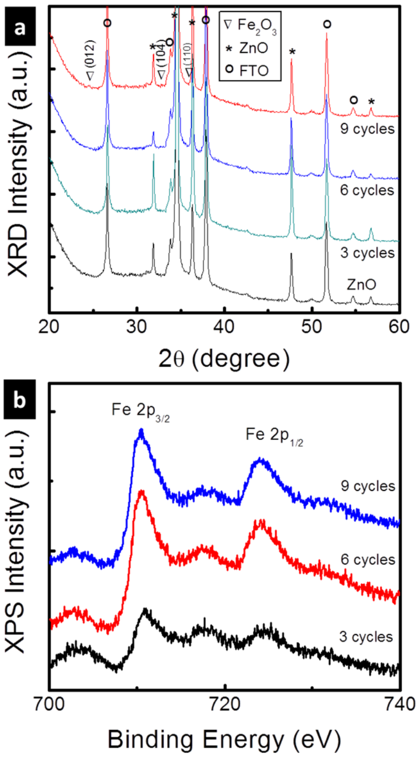

Figure 2. (a) X-ray diffraction patterns and (b) Fe 2p XPS spectra of ZnO/Fe_2O_3 core−shell NWs.

To elucidate the microscopic structure of the ZnO NW after deposition and annealing of α-Fe_2O_3, we conducted a detailed investigation using a field-emission transmission electron microscope (FE-TEM). Figure 3a shows a TEM image of a ZnO/Fe_2O_3 NW at small magnification. The surface of the ZnO NW is coated uniformly with a thin α-Fe_2O_3 shell (thickness ≈ 5 nm) after deposition and annealing for six cycles; the core−shell NW structure is confirmed. An image of the ZnO/Fe_2O_3 core−shell interface region at high resolution and a corresponding Fourier transform indicate that the polycrystalline α-Fe_2O_3 shell with lattice fringes due to planes (1−1−4) and (0−1−4) was deposited on the single-crystalline hexagonal ZnO NW grown along the c-axis of plane (0001)

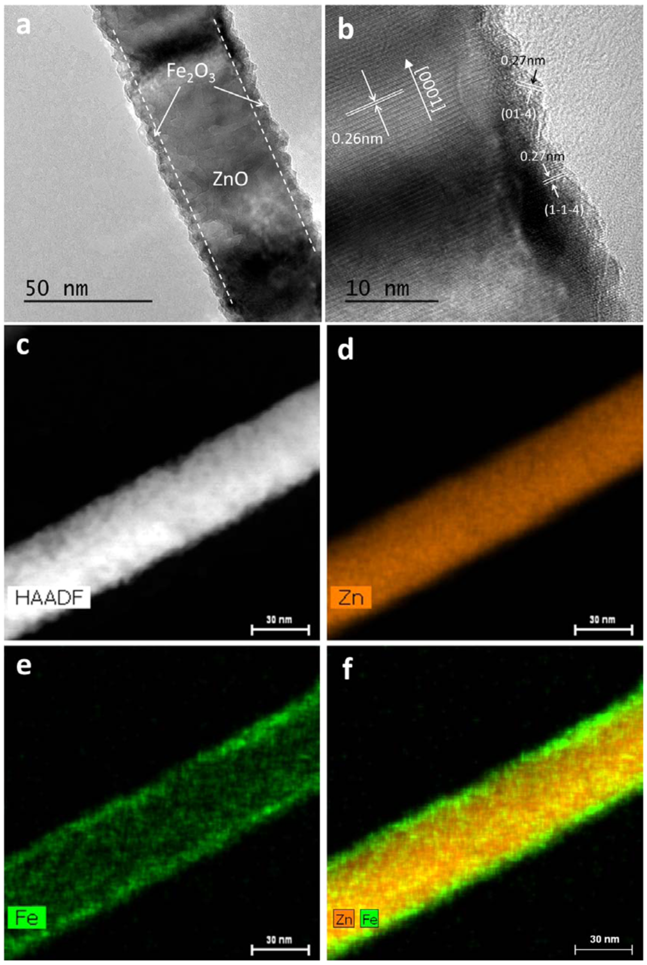

Figure 3. (a) Low magnification TEM image of a ZnO/Fe_2O_3 core−shell NWs. (b) High-resolution TEM image of the interface region of the ZnO/Fe_2O_3 core−shell NWs, showing a single crystalline wurtzite ZnO nanowire core and a polycrystalline cubic Fe_2O_3 shell layer. (c) HAADF image of the ZnO/Fe_2O_3 core−shell NWs, and the corresponding EDS elemental mapping of (d) Zn, (e) Fe, and (f) mixing Zn and Fe.

(Figure 3b). This finding is consistent with the XRD results. Figure 3c−f shows high-angle annular dark-field (HAADF) scanning TEM images of the middle part of a fractured ZnO/Fe_2O_3 core−shell heterostructure. The edge region clearly shows a cylindrical shell contrast of the Fe element, reflecting the overlapped double layers; the EDS elemental mapping confirmed the localized Zn element in the filled core area. These findings demonstrate that the α-Fe_2O_3 shell layer was completely stripped from the ZnO NW core.

3.2. PEC Performance of ZnO/Fe_2O_3 Core−Shell Electrodes.

To investigate the PEC characteristics of the ZnO/Fe_2O_3 core−shell NW that would make them suitable photoelectrodes for the solar generation of hydrogen from the decomposition of water, we used an electrochemical cell with three electrodes. For comparison, a linearly swept voltammogram of pristine ZnO NW and an α-Fe_2O_3 thin film on FTO after six cycles of deposition and annealing showed a small dark current, about 0.1 μA cm^{-2}, which indicated a non-Faradaic reaction, and photocurrents ~0.75 and ~0.5 mA cm^{-2} at 0.6 V, respectively (Figure 4). The photoinduced anodic current resulted from the oxidation of water involving the photogeneration of holes. The onset potentials of the ZnO NW and α-Fe_2O_3 thin film were notably approximately −0.5 and 0 V, respectively. When the surfaces of the ZnO NW were uniformly deposited with a thin layer of α-Fe_2O_3 as shell, the photocurrent increased significantly to 1.5 mA cm^{-2} after deposition of six cycles, and also exhibited a rapidly rising photocurrent. The photocurrent was doubled relative to bare ZnO NW. In addition, the electrochemical analysis of the different scan rate and stability were also performed (in SI Figure S2), and those results illustrated good characteristics in the photoelectrode. After deposition for nine cycles, the photocurrent slightly decreased as the thickness of the α-Fe_2O_3 layer increased; this effect might be ascribed to the small diffusion length of minority carriers and a small lifetime of photogenerated carriers in α-Fe_2O_3.[15,16] Relative to an α-Fe_2O_3 thin film, the onset potential of ZnO/Fe_2O_3 core−shell NW showed a significantly negative shift, which would benefit the solar decomposition of water at a smaller voltage. The photocurrent action spectra (Figure 5) show the efficiency of conversion of incident photons to electrons (IPCE) as a function of excitation wavelength at potential −0.2 V. This potential can manifest the advantage of ZnO/Fe_2O_3 core−shell NWs based on the characteristics of the negative onset potential and a rapidly rising photocurrent in comparison with bare Fe_2O_3 film. The photoresponses of the ZnO/Fe_2O_3 core−shell NWs and bare ZnO NWs show onset wavelengths of photocurrent generation about 600 and 390 nm, respectively, in the electrolyte. According to this comparison, the existence of an α-Fe_2O_3 shell layer is responsible for the conversion of visible light in agreement with the results of absorption spectra (in SI Figure S3). The gradual increase in the IPCE, η, with increasing photon energy is related to the energy of the band gap according to the following equation,[20]

$$\eta h\nu = A(L + W)(h\nu - E_g)^m \tag{1}$$

in which E_g is the band gap energy; exponent m = 1/2 for a direct and m = 2 for an indirect electronic transition; W is the width of the space-charge layer; and L is the diffusion length. The inset of Figure 5 shows that eq 1 with m = 2 is closely followed in a range of photon energies near the absorption threshold, indicating that the optical transition near the band gap is indirect. From the intercepts of the straight lines with the abscissal axis, the band gap energy for ZnO/Fe_2O_3 core−shell NW is found to be 2.1 eV, in agreement with literature reports.[10−14]

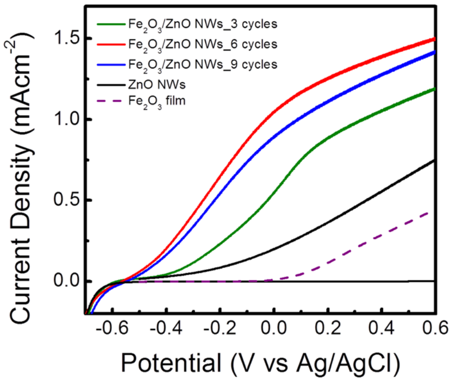

Figure 4. Photocurrent−voltage responses of the ZnO/Fe_2O_3 core−shell NWs.

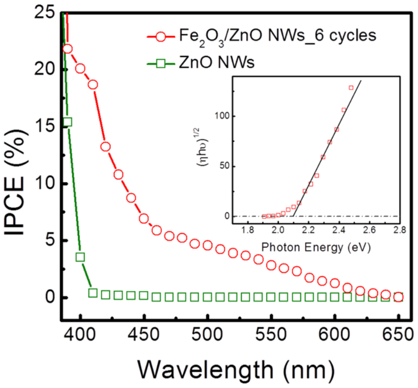

Figure 5. IPCE as a function of excitation wavelength at a potential of −0.2 V from ZnO/Fe_2O_3 core−shell NWs at 3 cycles of deposition-annealing procedure; inset, variation of the square root of IPCE (h) times hν with photon energy for ZnO/Fe_2O_3 core−shell NWs.

To probe detailed information about the energy band of a n/n heterojunction, we measured electrochemical impedance spectra on bare ZnO NW and an α-Fe_2O_3 thin film in darkness. To estimate the position of the flat-band potential for ZnO and α-Fe_2O_3, capacitances at the interface between semiconductor and electrolyte (SEI) with the use of an equivalent circuit are described with a Mott−Schottky plot. Figure 6, parts a and b, shows such a plot of data analyzed with CNLS fitting based on an equivalent circuit.[21] This Mott−Schottky equation relates the capacitance of a semiconductor to the carrier concentration (N_d) and to other constants and parameters, such as the fundamental electric charge e, relative permittivity (ε of ZnO is 8.5; ε of Fe_2O_3 is 80[19]), permittivity of vacuum (ε_o), temperature (T), Boltzmann constant (k_B), and the flat-band potential (V_{FB}).[21]

$$\frac{1}{C^2} = \left(\frac{2}{e\varepsilon\varepsilon_0 N_d}\right)\left[V - V_{FB} - \frac{k_B T}{e}\right] \tag{2}$$

That the slope of the linear part of the curve in the Mott−Schottky plot is positive indicates an n-type semiconductor. Plotting $1/C^2$ versus V allows the estimation of the flat-band potential and the concentration of surface carriers, the flat-band

DOI: 10.1021/acsami.5b03921
ACS Appl. Mater. Interfaces 2015, 7, 14157−14162

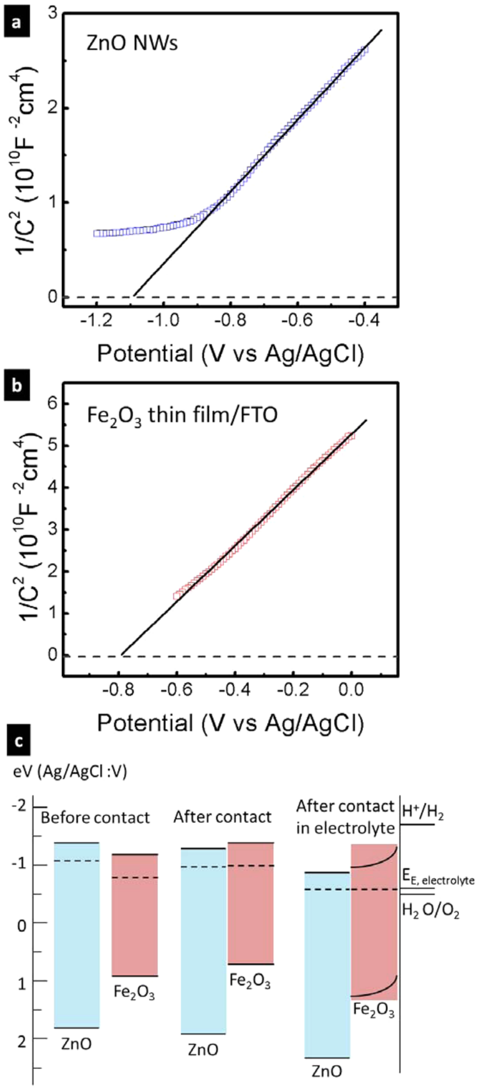

Figure 6. Mott−Schottky plot of (a) ZnO NWs and (b) α-Fe_2O_3 thin film. (c) Energy diagram of ZnO and α-Fe_2O_3 before and after contact.

potential calculated from the abscissal intercept and the carrier concentration from the slope. The values of the flat-band potential for ZnO and α-Fe_2O_3 are −1.09 and −0.79 V, respectively; estimation of the donor concentrations shows that, in ZnO and α-Fe_2O_3, the concentrations are 4.37×10^{18} and 2.65×10^{17} cm^{-3}, respectively. On the basis of the measured flat-band potential, carrier concentration, and energy of the band gap, the edges of the valence band and conduction band of ZnO and α-Fe_2O_3 before contact, together with the reduction and oxidation potentials of H_2O are shown in Figure 6c. Meanwhile, the conduction band of α-Fe_2O_3 is lower than that of ZnO, but the energy difference between the conduction band and Fermi level in Fe_2O_3 is larger than that of ZnO because of the higher carrier concentration of ZnO. After contact of the *n*/*n* heterojunction, ZnO has a work function greater than that of α-Fe_2O_3; the electrons in the Fermi level of ZnO thus migrate to the Fermi level of α-Fe_2O_3 until their Fermi levels equalize, which would make the conduction band of ZnO lower than that of α-Fe_2O_3, because of the smaller energy difference between the conduction band and Fermi level in ZnO. Therefore, under illumination, the photogenerated electrons in α-Fe_2O_3 can easily transport to ZnO, owing to the lower conduction band of ZnO. In addition, this *n*/*n* heterojunction might negatively raise the Fermi level of the core−shell NW and contribute to a negative shift of the onset potential of the ZnO/Fe_2O_3 core−shell nanoelectrode. This effect also caused a smaller external voltage to be required for the core−shell photoelectrode; the photocurrent began at a less positive potential relative to a bare Fe_2O_3 film. Furthermore, in contact with the electrolyte, under equilibrium conditions, the surface band bending becomes significant. This feature would further benefit the efficient separation of charge, resulting in rapid ramping of the photoresponse.

4. CONCLUSIONS

In this work, we used a simple chemical solution to fabricate core−shell photoelectrodes from ZnO/Fe_2O_3 NW arrays. The uniform coverages of an α-Fe_2O_3 shell at thickness a few nm and core diameter ∼80 nm of ZnO NW were confirmed with SEM and TEM. With XRD and XPS, we analyzed the structural and composition features of the ZnO/Fe_2O_3 core−shell NW. This *n*/*n* heterojunction structure would significantly cause a further negative shift of the flat-band potential and increase the surface band bending, relative to a bare α-Fe_2O_3 film electrode. These characteristics resulted in a doubling of photocurrent and a greater PEC stability at a less positive potential for the decomposition of water in a practical application. Our experiments improve our understanding of the heterojunction effect on PEC activity and provide a blueprint for the design of materials in the application of solar hydrogen.

■ ASSOCIATED CONTENT

Ⓢ Supporting Information

(Figure S1) The spectra of Xe lamp with and without A.M. 1.5 filter at the position of photoelectrode measured in the PEC analysis. (Figure S2) (a) Linear scan voltammograms of ZnO/Fe2O_3 core−shell NW electrode with potential scan rates of 50, 20, and 10 mV/s, in 1 M NaOH electrolyte. (b) Current density versus potential curves in the dark (black line) and in simulated AM 1.5 illumination for the ZnO/Fe_2O_3 core−shell NW array during the initial test (blue line) and after 1 h of illumination (red line). (Figure S3) Absorption spectra of bare ZnO NWs and ZnO/Fe_2O_3 core-shell NWs. The Supporting Information is available free of charge on the ACS Publications website at DOI: 10.1021/acsami.5b03921.

■ AUTHOR INFORMATION

Corresponding Authors

*Tel: +886-3-863-4196. Fax: +886-3-863-4180. E-mail: ykhsu@mail.ndhu.edu.tw (H.K.S.).
*Tel: +886-3-578-0281. Fax: +886-3-578-9816. E-mail: lin.yg@nsrrc.org.tw (H.G.L.).

Notes

The authors declare no competing financial interest.

■ ACKNOWLEDGMENTS

Ministry of Science and Technology, National Dong Hwa University, and National Synchrotron Radiation Research Center provided financial support under contracts MOST 103-2112-M-213-001-MY2, 103-2221-E-259-013 and 102T932, respectively.

REFERENCES

(1) Khaselev, O.; Turner, J. A. A Monolithic Photovoltaic−Photoelectrochemical Device for Hydrogen Production via Water Splitting. *Science* **1998**, *280*, 425−427.

(2) Hsu, Y. K.; Lin, Y. G.; Chen, Y. C. Polarity-dependent Photoelectrochemical Activity in ZnO Nanostructures for Solar Water Splitting. *Electrochem. Commun.* **2011**, *13*, 1383−1386.

(3) Boettcher, S. W.; Spurgeon, J. M.; Putnam, C.; Warren, E. L.; Turner-Evans, D. B.; Kelzenberg, D.; Maiolo, J. R.; Atwater, H. A.; Lewis, N. S. Energy-conversion Properties of Vapor−Liquid−Solid−Grown Silicon Wire-Array Photocathodes. *Science* **2010**, *327*, 185−187.

(4) Lin, Y. G.; Hsu, Y. K.; Chen, S. Y.; Lin, Y. K.; Chen, L. C.; Chen, K. H. Microwave-Activated CuO Nanotip/ZnO Nanorod Nanoarchitectures for Efficient Hydrogen Production. *J. Mater. Chem.* **2011**, *21*, 324−326.

(5) Huygens, I. M.; Strubbe, K.; Gomes, W. P. Electrochemistry and Photoetching of *n*-GaN. *J. Electrochem. Soc.* **2000**, *147*, 1797−1802.

(6) Pedro, S. Mechanisms of Water Photooxidation at *n*-TiO_2 Rutile Single Crystal Oriented Electrodes under UV Illumination in Competition with Photocorrosion. *Prog. Surf. Sci.* **2011**, *86*, 41−58.

(7) Hsu, Y. K.; Lin, C. M. Enhanced Photoelectrochemical Properties of Ternary $Zn_{1-x}Cu_xO$ Nanorods with Tunable Band Gaps for Solar Water Splitting. *Electrochim. Acta* **2012**, *74*, 73−77.

(8) AlOtaibi, B.; Nguyen, H. P. T.; Zhao, S.; Kibria, M. G.; Fan, S.; Mi, Z. Highly Stable Photoelectrochemical Water Splitting and Hydrogen Generation Using a Double-Band InGaN/GaN Core/Shell Nanowire Photoanode. *Nano Lett.* **2013**, *13*, 4356−4361.

(9) Hwang, Y. J.; Wu, C. H.; Hahn, C.; Jeong, H. E.; Yang, P. D. Si/InGaN Core/Shell Hierarchical Nanowire Arrays and their Photoelectrochemical Properties. *Nano Lett.* **2012**, *12*, 1678−1682.

(10) Qiu, Y.; Leung, S. F.; Zhang, Q.; Hua, B.; Lin, Q.; Wei, Z.; Tsui, K. H.; Zhang, Y.; Yang, S.; Fan, Z. Efficient Photoelectrochemical Water Splitting With Ultrathin Films of Hematite on Three-Dimensional Nanophotonic Structures. *Nano Lett.* **2014**, *14*, 2123−2129.

(11) Carroll, G. M.; Zhong, D. K.; Gamelin, D. R. Mechanistic Insights into Solar Water Oxidation by Cobalt−Phosphate-Modified α-Fe_2O_3 Photoanodes. *Energy Environ. Sci.* **2015**, *8*, 577−584.

(12) Steier, L.; Herraiz-Cardona, I.; Gimenez, S.; Francisco, F.; Bisquert, J.; Tilley, S. D.; Graetzel, M. Understanding the Role of Underlayers and Overlayers in Thin Film Hematite Photoanodes. *Adv. Funct. Mater.* **2014**, *24*, 7681−7688.

(13) Warren, S. C.; Voïtchovsky, K.; Dotan, H.; Leroy, C. M.; Cornuz, M.; Stellacci, F.; Hébert, C.; Rothschild, A.; Grätzel, M. Identifying Champion Nanostructures for Solar Water-Splitting. *Nat. Mater.* **2013**, *12*, 842−849.

(14) Bora, D. K.; Braun, A.; Constable, E. C. "In Rust We Trust". Hematite—The Prospective Inorganic Backbone for Artificial Photosynthesis. *Energy Environ. Sci.* **2013**, *6*, 407−425.

(15) Sivula, K.; Formal, F. L.; Graetzel, M. Solar Water Splitting: Progress Using Hematite (α-Fe_2O_3) Photoelectrodes. *ChemSusChem* **2011**, *4*, 432−449.

(16) Lin, Y.; Yuan, G.; Sheehan, S.; Zhou, S.; Wang, D. Hematite-Based Solar Water Splitting: Challenges and Opportunities. *Energy Environ. Sci.* **2011**, *4*, 4862−4869.

(17) Qi, X.; She, G.; Huang, X.; Zhang, T.; Wang, H.; Mu, L.; Shi, W. High-Performance *n*-Si/α-Fe_2O_3 Core/Shell Nanowire Array Photoanode Towards Photoelectrochemical Water Splitting. *Nanoscale* **2014**, *6*, 3182−3189.

(18) Mayer, M. T.; Du, C.; Wang, D. Hematite/Si Nanowire Dual-Absorber System for Photoelectrochemical Water Splitting at Low Applied Potentials. *J. Am. Chem. Soc.* **2012**, *134*, 12406−12409.

(19) Wang, G.; Ling, Y.; Wheeler, D. A.; George, K. E. N.; Horsley, K.; Heske, C.; Zhang, J. Z.; Li, Y. Facile Synthesis of Highly Photoactive α-Fe_2O_3-Based Films for Water Oxidation. *Nano Lett.* **2011**, *11*, 3503−3509.

(20) Hsu, Y. K.; Chen, Y. C.; Lin, Y. G.; Chen, L. C.; Chen, K. H. Birnessite-Type Manganese Oxides Nanosheets with Hole Acceptor Assisted Photoelectrochemical Activity in Response to Visible Light. *J. Mater. Chem.* **2012**, *22*, 2733−2739.

(21) Hsu, Y. K.; Yu, C. H.; Chen, Y. C.; Lin, Y. G. Fabrication of Coral-Like Cu_2O Nanoelectrode for Solar Hydrogen Generation. *J. Power Sources* **2013**, *242*, 541−547.

DOI: 10.1021/acsami.5b03921
ACS Appl. Mater. Interfaces 2015, 7, 14157−14162